Seismicity rate modeling for prospective stochastic forecasting: the case of 2014 Kefalonia, Greece, seismic excitation

D. Gospodinov, V. Karakostas, E. Papadimitriou

Nat Hazards (2015) 79:1039–1058
DOI 10.1007/s11069-015-1890-8

ORIGINAL PAPER

Seismicity rate modeling for prospective stochastic forecasting: the case of 2014 Kefalonia, Greece, seismic excitation

D. Gospodinov[1] · V. Karakostas[2] · E. Papadimitriou[2]

Received: 19 November 2014 / Accepted: 29 June 2015 / Published online: 10 July 2015

Abstract We examined the January–February 2014 earthquake doublet ($M_w = 6.1$ and $M_w = 6.0$) and the associated aftershocks which form a seismic excitation adequately well recorded by a dense local seismological network. It started on January 26 with the main shock, causing a lot of panic and followed by numerous aftershocks. The second main shock with $M_w = 6.0$ occurred 7 days later on an along-strike adjacent fault segment. The close proximity of the two main shocks, in both space and time and the intense aftershock sequence, triggered the investigation of the occurrence probability evolution for the stronger aftershocks and possibly a third main shock in the seismic excitation. This purpose was further motivated by the potential of the area for hosting a stronger ($M_w \geq 6.0$) earthquake based upon both historical information and instrumental data. Aftershock rate modeling was done on subsequent data samples by the restricted epidemic-type aftershock sequence stochastic model, and probabilities for the occurrence of strong ($M_w \geq 5.0$) earthquakes were calculated during the progress of the aftershock sequence. We executed daily model simulations and probability forecasts for 30 days focusing in more detail on the impact of some model parameters on the prospective forecasting. Trying to be near to a real-time case, all forecasts were done on data up to the moment of forecasting.

Keywords Seismicity · Aftershock sequence · Aftershock probabilities · Kefalonia (Greece) · RETAS stochastic model

✉ D. Gospodinov
drago@uni-plovdiv.bg

V. Karakostas
vkarak@geo.auth.gr

E. Papadimitriou
ritsa@geo.auth.gr

[1] Faculty of Physics, Plovdiv University "Paisii Hilendarski", 4000 Plovdiv, Bulgaria

[2] Geophysics Department, Aristotle University of Thessaloniki, 54124 Thessaloníki, Greece

1 Introduction

On 26 January, 2014, an earthquake of $M_w = 6.1$ struck the western part of Kefalonia Island, Greece, causing severe damage to the infrastructures and a lot of panic to the inhabitants. Almost a week later, on February 3, a second strong earthquake of $M_w = 6.0$ occurred with its epicenter being located approximately 7 km to the north of the first one. Both shocks were followed by numerous aftershocks increasing even more the feeling of anxiety and the willingness of people to know more about the ongoing seismic activity. The properties of the seismic sequence were studied by the use of precise aftershock locations resulted from the recordings of a dense digital seismic network (Karakostas et al. 2014a). These authors also presented evidence of seismicity triggering in the along-strike adjacent fault segment, due to the static stress changes from the first main shock. The accurately located aftershocks illuminated for the first time the position of the causative fault, which bounds the Island's western coastlines, thus shading more light on the hazard associated with the largest earthquakes of this region.

The along-strike activated adjacent fault segments consist parts of the Kefalonia Transform Zone (KTFZ) and are located along the Palliki Peninsula (Fig. 1). This zone exhibits the highest rate of large earthquakes (up to $M_w^* = 7.4$ from historical information, M_w^* being the equivalent moment magnitude; see Papazachos and Papazachou 2003), having hosted about 10 $M_w^* \geq 6.0$ earthquakes every century. The exceptional high rate results from the relatively fast tectonic loading ($\sim$30 mm/yr, McClusky et al. 2000), whereas Coulomb stress interactions seem to play a role in the location and timing of earthquakes in this area (Papadimitriou 2002), which appear to cluster in time. The most prominent cluster was the one of 1953 when three earthquakes of $6.4 \leq M_w^* \leq 7.2$ have

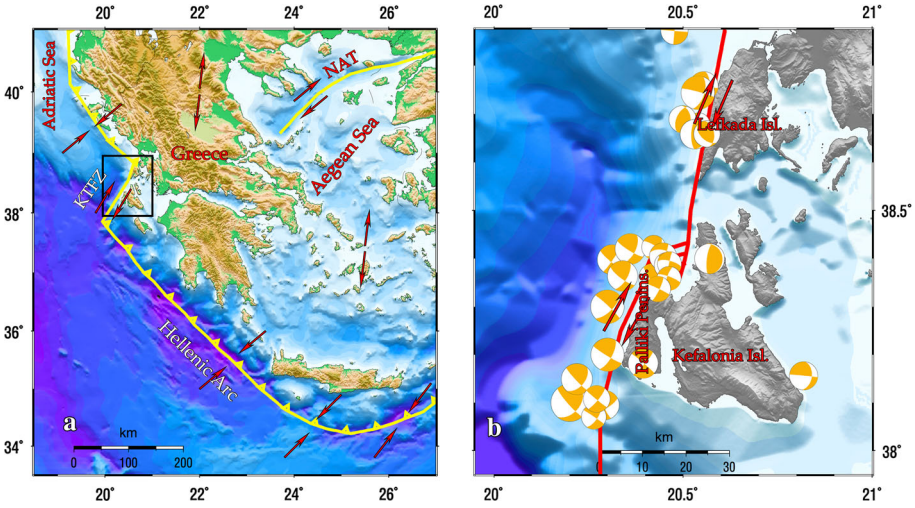

Fig. 1 **a** Main geodynamic features of the Aegean and surrounding areas. The active boundaries are shown as *solid lines*. The *arrows* indicate the approximate direction of relative plate motion. The study area is denoted by the *square*. *KTFZ* Kefalonia Transform Fault Zone, *NAT* North Aegean Trough. **b** Main active boundaries in the area of central Ionian Islands. The dextral strike-slip Kefalonia and Lefkada fault segments are traced (forming the Kefalonia Transform Fault System). The most reliable available fault plane solutions of the strong earthquakes that occurred in the area in the last four decades are shown as *lower hemisphere* equal area projections

occurred in 3 days apart (9–12 August 1953) and have turned important cities and smaller villages in Kefalonia and the adjacent to the south Zakynthos Island (Fig. 1) into piles of rubble.

Given the cascade-type occurrence of strong destructive main shocks as in the aforementioned case, along with the high rate of the aftershock occurrence and in particular shortly after the main shock occurrence, the seismicity rate modeling is an indispensable component for any mitigation plan. Probability evolution analysis of aftershocks is one of the first steps toward establishing an integrated decision-making support framework for emergency management in the case of a seismic excitation. The probability assessment has become feasible on the basis of seismicity models, developed to represent spatiotemporal distribution of earthquakes. Statistical and physical models on earthquake interactions (Ogata 1988, 1998; Gospodinov and Rotondi 2006; Console et al. 2006a, 2007; Özel 2011) have begun to capture many features of natural seismicity, such as aftershock triggering and clustering.

The short-term stochastic models provide the tools to perform an assessment of aftershock occurrence probabilities with applications worldwide (Reasenberg and Jones 1989, 1994; Jordan et al. 2011) and in aftershock sequences in Greece (Drakatos and Latoussakis 1996; Latoussakis et al. 1991; Papadimitriou et al. 2013; Karakostas et al. 2014b). These models demonstrate a probability gain in forecasting future earthquakes relative to the long-term, time-independent models typically used in seismic hazard analysis. In their papers, Reasenberg and Jones (1989, 1994) introduced an algorithm for calculating the occurrence probability in a sequence of at least one aftershock above certain magnitude level. The algorithm is grounded on a hazard model composed of two components to determine the rate of the larger magnitude aftershocks. The first component depicts the temporal decay of aftershock rate, and the second one analyzes aftershocks energy distribution. In these studies, the modified Omori formula (MOF) was selected to represent aftershock distribution in time (Utsu 1961) and the Gutenberg–Richter law for magnitude distribution (Gutenberg and Richter 1944). The stochastic models became more complex later on for comprising spatial distribution. The most popular among them are the epidemic-type aftershock sequence (ETAS) model (Ogata 1988, 1998) and the short-term earthquake probability (STEP) model (Gerstenberger et al. 2005, 2007). Recent attempts are targeted to calculations of the nearly real-time aftershock occurrence probabilities and in particular the ensuing strongest ones. Marzocchi and Lombardi (2009) were among the first to carry out daily prospective forecasts of aftershocks after the 2009 L'Aquila earthquake in Italy, based mainly on the ETAS model with some parameters being estimated from beforehand seismicity.

In this study, the RETAS model (Gospodinov and Rotondi 2006; Gospodinov et al. 2007) was selected for investigating events temporal evolution, because it provides the ability of identifying the most appropriate among a number of model versions for best fitting the data, among them MOF and ETAS being the limit cases. All necessary model parameters for the execution of the occurrence probability calculations were estimated on data samples that comprise aftershocks occurring up to the end of each day. From the beginning, the interest was focused upon the possible options for the evolution of the aftershock sequence. A possible scenario could be that an earthquake up to $M_w = 7.0$ could follow the first main shock. Given that this case was a real fact in the past not only in the study area (1953 seismic paroxysm) but also in other places as well (for example, 1978 in Thessaloniki; 1997 in Umbria–Marche), it was important to analyze this contingency. Keeping this magnitude as the ceiling, different possible scenarios were examined for anticipated earthquakes in the magnitude range between 5.0 and 7.0. By choosing to consider also developments, in which the strongest earthquake in the sequence is still anticipated, we proceed beyond modeling of

only aftershock activity and have to take into account the activity preceding a strong earthquake. This task can be solved using various models. The noncritical precursory accelerating seismicity theory (N–C PAST, Mignan et al. 2007; Mignan 2012) and the accelerated seismic release (ASR) model (Ben-Zion and Lyakovsky 2002) focus on seismicity patterns before strong earthquakes, based on the idea that small events are the signature of ongoing loading on a fault that will host the future mainshock (i.e., top-down loading process). This view is quite far from the prevailing concept of complexity in the field of earthquake prediction, which is based on the understanding that small events cascade into the largest one by a bottom-up triggering process. In this study, the authors have chosen to analyze the activity in the sequence by a model with a decreasing hazard function with the purpose to forecast the evolution of occurrence probability of strong events in the sequence on the grounds of aftershocks rate decay.

2 The seismic sequence of January–February 2014

The first main shock with $M_w = 6.1$ occurred on January 26, 2014, at the southern part of Palliki peninsula (depicted by yellow star in Fig. 2a), causing considerable damage and followed by an intense seismic sequence that lasted for several months. Figure 2a shows

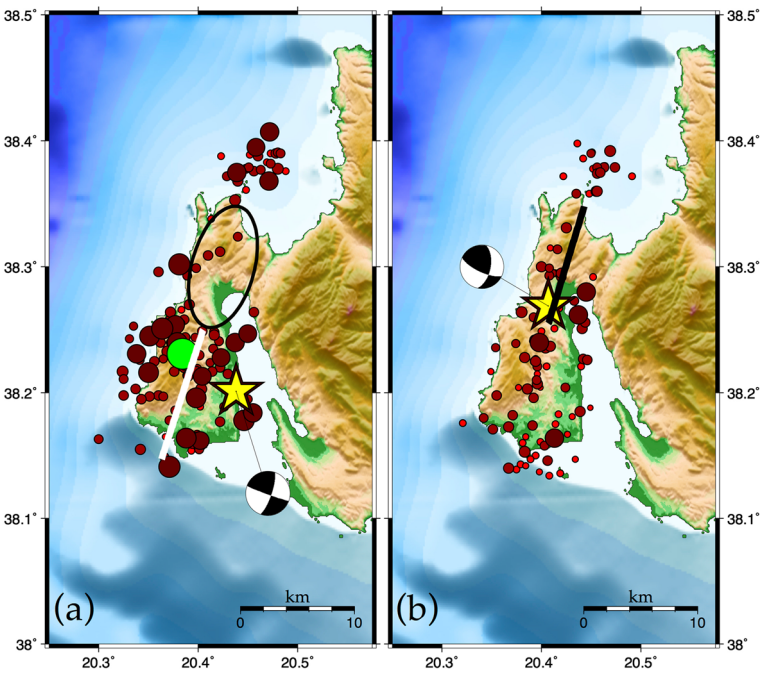

Fig. 2 **a** Seismicity of the first 24 h after the occurrence of the $M_w = 6.1$ main shock on January 26, 2014. **b** Seismicity of 24 h after the occurrence of the second strong earthquake with magnitude $M_w = 6.0$ on February 03, 2014. *Yellow stars* depict the main shocks epicenters, *big green circle* the largest aftershock, whereas aftershock epicenters are depicted by *circles* the size of which is proportional to the corresponding magnitude. The *lines* indicate the inferred surface fault traces, whereas the ellipse emphasizes a low seismicity area before the occurrence of the second main shock

the relocated aftershocks of the first 24 h, with the largest aftershock of $M_w = 5.5$ (green circle in Fig. 2a) occurring in the first few hours. This aftershock activity occupied an area expanding in about 35 km from the southernmost part of Palliki peninsula to the offshore area north of it, having a SSW–NNE orientation, and can be divided into three clusters. The southern cluster, encompassing the most intense seismic activity, defines an area with a length of about 12 km (the inferred fault trace is shown by the white line in Fig. 2a) as anticipated for an $M_w = 6.1$ strike-slip earthquake (Wells and Coppersmith 1994; Papazachos et al. 2004). The area marked with an ellipse accommodates the lowest seismicity in the first days of the sequence with a few small-magnitude aftershocks. Further to the north, however, an offshore cluster with rather low magnitude earthquakes was developed. An interpretation based upon the epicentral distribution attributes this pattern to the first rupture with a length of 12 km, being stopped due to a strong asperity coinciding with the low seismicity area (Karakostas et al. 2014a).

Almost a week later (3 February 2014), a second main shock of $M_w = 6.0$ occurred just north of the southern cluster and at the southernmost part of the area that has been recognized as an unbroken asperity after the first main shock occurrence. The second main shock (yellow star in Fig. 2b) is associated with the adjacent along strike and almost equal in length fault segment (black line in Fig. 2b). Aftershock activity for the 24 h after the second strong earthquake filled in the gap that highlighted from the first day seismicity, although the activity again was not significant. The length of the second rupture is about 10 km, in agreement with the aforementioned scaling laws for strike-slip faulting. Due to stress transfer associated with the coseismic slip of the second strong earthquake, seismicity is continued in the other two clusters, associated with two segments that belong to the main tectonic feature in this area, the right lateral Kefalonia Transform Fault (KTF). The offshore seismicity is the result of either static or dynamic triggering of smaller faults, which strike obliquely to the KTF. Later on Sakkas and Lagios (2015), using geodetic data, proposed a rupture model of two segments in agreement with Karakostas et al. (2014a).

Figure 3 shows the relocated aftershocks up to the end of June 2014. Relocation was performed by hypoinverse and the double difference technique using appropriate velocity model and station corrections (Karakostas et al. 2014a). The phase data are included in the monthly bulletins of the Geophysics Department of the Aristotle University of Thessaloniki. In addition to the recordings of the Hellenic Unified Seismological Network (HUSN), the recordings of accelerometers installed by the Institute of Engineering Seismology and Earthquake Engineering (ITSAK) inside the affected area were used.

Based on the more than 5-month spatial distribution of the aftershock activity, it is concluded that most of the seismic energy was released in the southern part of the aftershock zone, hosting the first main shock and two shocks of $M_w = 5.0$ and $M_w = 5.5$. In addition to the main rupture, other smaller active structures have been activated that contributed in increasing the dimensions of the aftershock zone. The idea of a homogeneous asperity that was broken during the second strong earthquake in the middle part of the aftershock zone is supported by the narrow zone of the aftershocks at this location. Finally, the third offshore cluster is very clearly discriminated from the central and southern clusters. Taking also into account the seismicity of the last decade, it is believed that seismicity in this area is connected with smaller faults, which create a step over faults dividing the KTFZ into a north and a south branch (Karakostas et al. 2014a).

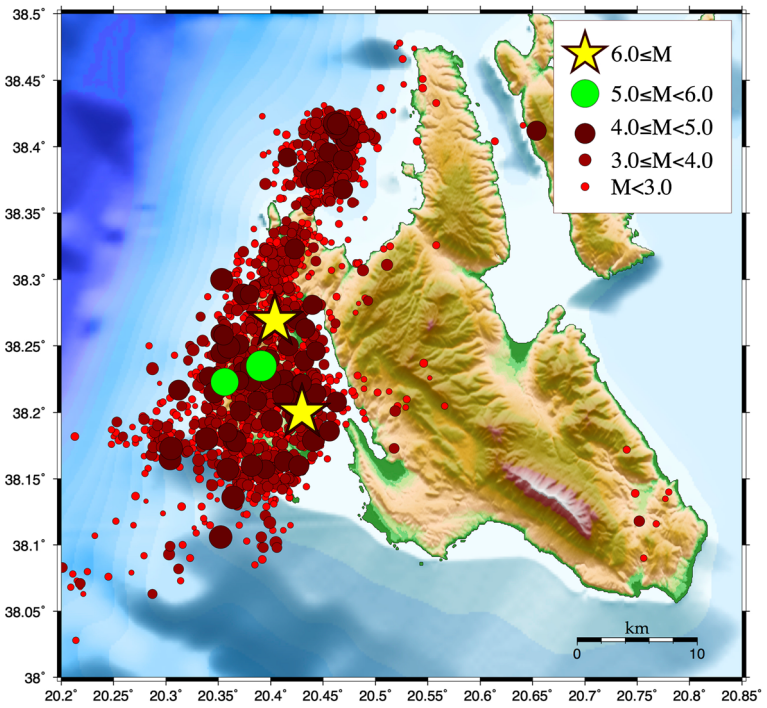

Fig. 3 Spatial distribution of the relocated aftershocks until the end of June 2014. *Symbols* are the same as in Fig. 2

3 The RETAS model as a basis for short-term probability forecasts

Short-term probability forecasts (days to weeks) for aftershock occurrence in the course of a seismic sequence are based on two key groups of seismicity models. The first of them comprises a number of stochastic models of aftershock rate decay in time and space. Among them, the MOF and ETAS models are the most widely used for subsequent occurrence probability calculations (Reasenberg and Jones 1989; Marzocchi and Lombardi 2009; Marzocchi et al. 2012). The second group concerns models that study the magnitude distribution of earthquakes, the so-called Gutenberg–Richter law (Gutenberg and Richter 1944) being used most often.

Historically, the MOF is the first model of aftershock rate decay, according to which the aftershock frequency per unit time is given by the inverse power law (Utsu 1961):

$$n(t) = \frac{K}{(t+c)^p} \tag{1}$$

where t is the time elapsed since the main shock occurrence, K is a parameter related to the main shock magnitude and to the cut-off magnitude M_0, p is a coefficient of attenuation and c is the time-offset parameter, i.e., the time delay before the onset of the power-law aftershock decay rate (Holschneider et al. 2012). The frequency $n(t)$ in (1) can be considered as the conditional intensity function of a point process, i.e.,

$$n(t) \approx \lambda(t) \tag{2}$$

where $\lambda(t)$ signifies

$$\Pr\{\text{an event occurs in } (t, t+\mathrm{d}t)|H_t\} = \lambda(t|H_t)\mathrm{d}t + o(\mathrm{d}t). \tag{3}$$

Here H_t is the history of the process, which for the MOF is only the main shock occurrence time, because the model is grounded on the concept that the entire relaxation process is controlled by the stress changes caused by the main shock alone. The aftershocks are conditionally independent and follow a nonstationary Poisson process. The MOF model fits well the data of simple aftershock sequences, but quite often there are earthquakes in a sequence, which cause secondary clustering. Such compound cases with one or more secondary aftershock sequences led Ogata (1988) to consider aftershock clustering as a self-similar process, where all aftershocks can induce further aftershocks, the triggering capacity depending on their magnitude. The model was called the ETAS model, and its conditional intensity function is:

$$\lambda(t|H_t) = \mu + \sum_{t_i<t} \frac{K_0 e^{\alpha(M_i - M_0)}}{(t - t_i + c)^p}. \tag{4}$$

In this equation, μ is the background seismicity rate, the history H_t consists of the times t_i (days) and magnitudes M_i of all events occurred before t, and the summation includes all events with occurrence times $t_i < t$ and magnitudes equal to or stronger than the lower cut-off, M_0. The parameters c and p are defined as the ones in the MOF and K_0 is a multiplier, common to all aftershocks, which has an impact on the total aftershock productivity. In Eq. (4), every addend represents the contribution of a previous event to the occurrence probability of subsequent events at time t; it is composed of two factors: the temporal decay rate, presented by MOF, and the exponential term $e^{\alpha(M_i - M_0)}$, chosen upon the base of the linear correlation between the logarithm of the aftershock area and the main shock's magnitude (Utsu and Seki 1955). Here α measures the effect of magnitude in the production of "descendants."

The MOF and the ETAS models expressed by Eqs. (1) and (4), respectively, present two limit cases to model the temporal distribution of an aftershock sequence. The former assumes one event (the main shock) to trigger all aftershocks without any interaction among them and the latter assumes that both the main shock and all aftershocks can trigger events of subsequent generations. There is a group of trigger models, allocated between MOF and ETAS and considering similar behavior (Ogata 2001). For many sequences, however, only some events trigger additional seismicity, typically being some of the stronger aftershocks, a case not covered by the MOF and the ETAS models. To fill in the gap, Gospodinov and Rotondi (2006) developed a trigger model based upon the assumption that not all events in a sample but only aftershocks with magnitudes larger than or equal to a threshold M_{th} can induce secondary seismicity. Then, the conditional intensity function for the model is formulated as

$$\lambda(t|H_t) = \mu + \sum_{\substack{t_i<t \\ M_i \geq M_{th}}} \frac{K_0 e^{\alpha(M_i - M_0)}}{(t - t_i + c)^p}. \tag{5}$$

The history H_t in the latter formula consists only of the times t_i (days) and the magnitudes M_i of the earthquakes occurred before t with $M_i \geq M_{\text{th}}$. All other parameters are similar to the ones in the ETAS model expressed by (4), and this similarity along with the above restriction motivated the model expressed by (5) to be named as the RETAS model.

RETAS is similar to the original trigger model (Ogata 2001), but the definition of a primary event (an earthquake, capable of triggering aftershocks) here differs from the one in the original model, in that a primary shock here can be triggered by preceding events, whereas in the latter model the primary events are independent and follow a stationary Poisson process. The RETAS model assumes possible interaction between aftershocks in a set, allowing each one of them with magnitude $M_i \geq M_{\text{th}}$ to be capable to induce further shocks of subsequent generations. All events with magnitudes smaller than M_{th}, however, are excluded from the triggering process, and they are regarded only as "descendants." This model is advantageous, in that the gap between M_{th} and M_0 is not fixed and by varying M_{th}, all RETAS versions between the MOF and the ETAS model (including them as two limit versions) can be examined on the basis of the Akaike information criterion (AIC) (Akaike 1974), given by

$$\text{AIC} = -2\max \log L(\theta) + 2k \tag{6}$$

where θ stands for the model parameters, k is the number of model parameters and $\log L$ is the logarithm of the likelihood function

$$\log L(\theta) = \sum_{i=1}^{N} \log \lambda_\theta(t_i|H_{t_i}) - \int_0^T \lambda_\theta(t|H_t)\mathrm{d}t. \tag{7}$$

Here H_{t_i} (history at time t_i) are defined as in Eq. (4) and N is the number of events in the sample. Allowing the triggering magnitude M_{th} to vary from the cutoff, M_0, up to the main shock magnitude, a number of RETAS model versions are considered with the smallest value of the Akaike criterion revealing the best-fit model (Akaike 1974). Considering the above-mentioned features of the RETAS model, the most important being the provision of a number of model versions for choosing the one best fitting the data and also that it includes the MOF and the ETAS models in the analysis, its application was decided in the present study for modeling the aftershock temporal distribution. RETAS model simulations were also executed for calculating aftershock occurrence probabilities.

The power-law describing the earthquake magnitude distribution necessary for the aftershock probability calculations is (Gutenberg and Richter 1944)

$$\log_{10} N(M) = a - bM \tag{8}$$

where a is the productivity constant, b reflects the ratio of small to large events and depends upon the material heterogeneity (Mogi 1962), and N is the number of events with magnitudes larger than or equal to magnitude M. Combining formulae (1), (2) and (8), Reasenberg and Jones (1989, 1994) developed a hazard model as

$$\lambda(t, M) = \lambda(t)S(M). \tag{9}$$

where t is the time since the main shock, $\lambda(t)$ is the aftershock rate, and $S(M)$ is the probability of the magnitude being greater than or equal to M, given by

$$S(M) = \exp\{-\beta(M - M_0)\} \tag{10}$$

where M_0 is the cutoff magnitude, and $\beta = bln10$ [b from Eq. (8)]. If the temporal model is the MOF and both power laws [Eqs. (1), (2) and (8)] were combined, then the Eq. (9) turns to (Reasenberg and Jones 1989):

$$\lambda(t, M) = 10^{a+b(M_{\text{m}}-M)}(t + c)^{-p} \tag{11}$$

Here t is the time since the main shock occurrence with magnitude M_m. The hazard model, represented by Eq. (11), can be alternatively given on the basis of Eq. (9). For a nonstationary Poisson process, the probability P for at least one aftershock of magnitude between M_1 and M_2, to occur in the period (T_1, T_2) after the main shock, is given by:

$$P(M_1, M_2; T_1, T_2) = 1 - \exp\left[- \int_{M_1}^{M_2} \int_{T_1}^{T_2} \lambda(t, M) \mathrm{d}M \, \mathrm{d}t \right] \tag{12}$$

For more complex sequences, where the best-fitting model is different from the MOF, we still may calculate the integrals in Eq. (12) and thus obtain probability estimates, under the assumption that future aftershocks will follow the same temporal model and magnitude distribution as the ones that have already occurred. The aftershock rate for the considered period, however, will depend not only on the already existed earthquakes but also on events that will occur in the study period. In this case, for a prospective probability forecast to be made at time t, a Monte Carlo simulation of the RETAS model must be performed after this time (Gospodinov and Rotondi 2006; Gospodinov et al. 2007; Papadimitriou et al. 2013; Karakostas et al. 2014b) using the calculated model parameters MLEs and the b value estimate from Eq. (8). Then formula (12) will provide the anticipated probability.

4 Daily forecasts of occurrence probabilities

Calculations of occurrence probabilities were performed for daily forecasts of strong events in the magnitude ranges $M_w = 5.0$–6.0, $M_w = 5.0$–6.5 and $M_w = 5.0$–7.0. Aiming to imitate prospective forecasting, calculations were based only on data available up to the time when the forecast is pertained. It concerns a short-term forecasting, although implemented retrospectively and not in real time. True real-time prospective forecasts were provided by Marzocchi and Lombardi (2009) and Marzocchi et al. (2012) for L'Aquila and Emilia earthquake sequences, respectively, with their model being calibrated on data before the main shock occurrence, as we have already mentioned in the introduction section. A number of models for short-term forecasting are presently under test in some experiments within the Collaboratory for the Study of Earthquake Predictability (CSEP) (Jordan 2006; Schorlemmer et al. 2007), which, however, are not designed to evaluate the real-time models performance but require a certain time lag for provisional seismicity catalogs to be corrected and finalized. Short-range forecasting models were attempted and fitted to the earthquake catalog of Greece by modeling temporal and spatial variations of $M \geq 4.0$ earthquake occurrence rate for forecasting events of $M_w \geq 6.0$ and revealed that the preparation of a major earthquake is often signaled by precursory changes in the patterns of earthquake occurrence in time, space and magnitude (Console et al. 2006b).

The RETAS model estimates the seismicity rate accounting for the triggering effect of the past events in a sequence above a magnitude threshold. A reliable forecast of the expected number of events in a forecasting time window (1 day in our case) requires accounting for the triggering effect of all these events that occurred before the forecasting starting time and for the ones that will occur during the forecasting time window, the latter being simulated by the model. We performed the following steps in our investigation:

(a) Compilation of cumulative datasets at the end of each day
(b) Initial statistical analysis of each dataset

(c) RETAS model analysis and identification of the best-fit model for the sample
(d) Simulation of the identified best-fit model for the next day (24 h)
(e) Applying Eq. (12) to calculate occurrence daily probability of at least one event in a certain magnitude range
(f) Repeating all previous steps subsequently for 30 days after the beginning of the sequence.

Going into details for the first step, we defined subsequent data sets from the catalog, prepared for the purpose of this study as it was described in the seismic sequence section, each of them covering the period from the start of the sequence until the end of the day before making the forecast. We did not prepare a data set for the first day only (first data sample is for the first 2 days), because of insufficient number of events.

Then the sample was analyzed (step b) using the ZMAP software (Wiemer 2001) to determine the completeness magnitude, M_0, and the b value (Eq. 8). Figure 4 shows a graph of this analysis for a randomly chosen sample (first 11 days). It can be seen that stronger aftershocks are less than predicted from the G–R curve (the magnitude range comprised into the circle in Fig. 4), an observation found in nearly all catalogs. For the simulated catalogs, however, which were generated after the estimated b values, there would not be such a deviation, which is reflected in aftershock rate overestimation by the model, as will be further identified (as we will see in Fig. 5).

After defining the completeness magnitude M_0 for a certain sample [step (c)], we excluded all events weaker than M_0 for the corresponding sample and analyzed the rest through the RETAS model (the background rate μ was assumed to be zero for all samples). The minimum value of AIC (Eq. 6) then recognizes the model version, which best fits the data set, providing also the MLEs of the model parameters (Table 1). All four model parameters vary for the different best-fit models, which were identified for the subsequent data sets, although only p and b values are shown in Table for the sake of simplicity and since these are the most often considered in aftershock decay studies.

For executing step (d), we simulated the best-fit model for the next day (24 h). The simulation was done within a certain magnitude range—the lower limit is equal to the determined M_0 and the upper limit is selected to verify the different possible scenaria, the maximum upper limit being determined by the potential of the study area, in our case $M_{\max} = 7.0$.

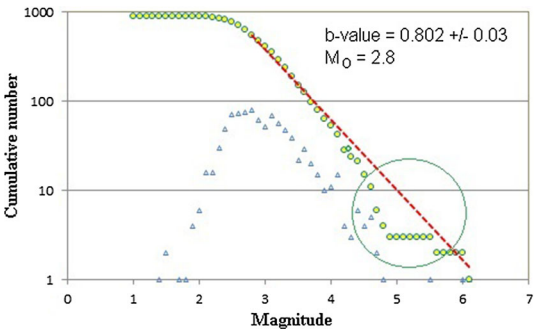

Fig. 4 Magnitude distribution of the catalog data for the first 11 days, along with the completeness magnitude, M_0, definition and b value estimation. *Squares* stand for the cumulative distribution, and triangles represent the noncumulative one. The area encompassed by the *dashed contour* reveals a lack of observed stronger aftershocks, compared to the expected by the fitting of the straight line

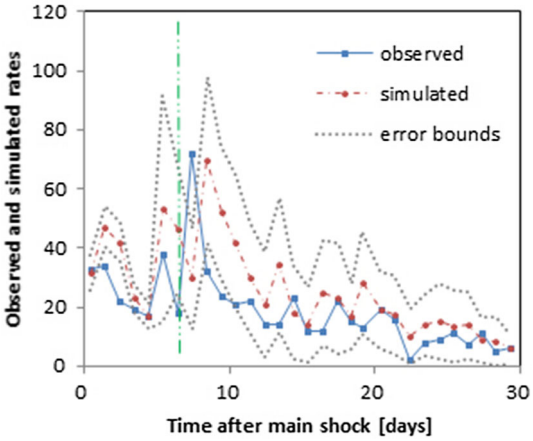

Fig. 5 Observed (*continuous line*) and simulated (*dashed line*) daily aftershock rate above the completeness magnitude, M_0, defined for each day. The *vertical line* shows the occurrence time of the second main shock. The *dotted lines* represent the standard deviation error bounds

To forecast the aftershock rate for the day (24 h) next to the one up to which the corresponding data sample was prepared [step (d)], we had to consider all occurred events stronger than or equal to the magnitude threshold M_{th} and the ones that would occur during the next 24 h. We accomplished this step by Monte Carlo simulation of the identified best-fit model. For each forecast, 1000 different synthetic 1-day catalogs were simulated by following the thinning method (Ogata 1998). We can apply two approaches to simulate the daily rate. At each time t (in days), we may simulate 1000 realizations of the best model; for each i-th simulation, $i = 1, \ldots, 1000$, we have N_i events at times j and with magnitudes M_j, $j = 1, \ldots, N_i$. As in the point processes $E[N(0,t)|H_t] = \int_0^t \lambda(u|H_u)\mathrm{d}u$, that is, the expected number of events in the interval $(0, t)$ is given by the cumulative intensity function $\Lambda(t)$, one can evaluate, every day t, the expected rate of the next day, $\hat{\lambda}^{(t+1)}$ $i = 1, \ldots, 1000$ by integrating (6) over $(t, t + 1)$ conditioned on the history H_t plus the simulated part (obtaining in this way the history H^i_{t+1}), and then compute the average $N^{(t+1)} = \sum_{i=1}^{1000} N_i^{(t+1)}/1000$. Otherwise, one can use the simulated number of events $N_i^{(t+1)}$ and compute the average $N^{(t+1)} = \sum_{i=1}^{1000} N_i^{(t+1)}/1000$. We have applied the latter approach, subsequently simulating events and including them in the extended data sample for the new simulation until the time exceeds 24 h and then taking the average and the standard deviation from the full empirical distribution of the simulated rates, the standard deviation being used to form the error bounds.

After that, for implementing step (e), we took the simulated average rate to stand for $\int_{t_i}^{t_i+1} \lambda(t, M)\mathrm{d}t$ in Eq. (12), and by integrating it in the chosen magnitude range, we calculated the occurrence probability of at least one event in this range to occur in the next day. We repeated all above operations [step (f)] subsequently for 30 days after the beginning of the sequence.

The above considerations imply that probability values are influenced by the parameters involved in the calculations, as the completeness magnitude, M_0, the selected magnitude range for the simulation, the b value and the best-fit model parameters. When comparing probabilities assigned to different days, we have to keep in mind that they were calculated after different values of the aforementioned parameters. Since M_0 is not the same for the entire study period but it changes every day, this is reflected to the simulated aftershock rates.

Table 1 Results from the RETAS analysis performed for the data samples at the end of each day (b and p values are the ones from Eqs. (9) and (6), respectively

Forecast date	b value	Aftershocks number (N)	Best-fit model	1-Day aftershock occurrence probability of at least one event in the corresponding magnitude range		
	p value	Completeness magnitude (M_0)		M_w 5.0–7.0	M_w 5.0–6.5	M_w 5.0–6.0
Jan. 28 2014	$b = 0.86$ $p = 0.514$	$N = 123$; $M_0 = 3.2$	MOF $M_{th} = 6.1$	0.798	0.773	0.738
Jan 29 2014	$b = 0.828$ $p = 0.5527$	$N = 190$; $M_0 = 3.1$	MOF $M_{th} = 6.1$	0.747	0.716	0.673
Jan 30 2014	$b = 0.865$ $p = 1.171$	$N = 212$; $M_0 = 3.1$	MOF $M_{th} = 6.1$	0.482	0.452	0.412
Jan 31 2014	$b = 0.881$ $p = 1.386$	$N = 231$; $M_0 = 3.1$	MOF $M_{th} = 6.1$	0.339	0.321	0.3
Feb 1 2014	$b = 0.759$ $p = 1.497$	$N = 371$; $M_0 = 2.8$	RETAS $M_{th} = 4.3$	0.73	0.706	0.68
Feb 2 2014	$b = 0.781$ $p = 1.153$	$N = 409$; $M_0 = 2.8$	RETAS $M_{th} = 3.1$	0.627	0.615	0.588
Feb 3 2014	$b = 0.798$ $p = 1.173$	$N = 427$; $M_0 = 2.8$	RETAS $M_{th} = 3.1$	0.438	0.429	0.407
Feb 4 2014	$b = 0.784$ $p = 1.182$	$N = 499$; $M_0 = 2.8$	RETAS $M_{th} = 3.1$	0.732	0.753	0.732
Feb 5 2014	$b = 0.796$ $p = 1.175$	$N = 531$; $M_0 = 2.8$	RETAS $M_{th} = 3.1$	0.643	0.633	0.604
Feb 6 2014	$b = 0.802$ $p = 1.287$	$N = 555$; $M_0 = 2.8$	RETAS $M_{th} = 2.9$	0.543	0.534	0.514
Feb 7 2014	$b = 0.807$ $p = 1.346$	$N = 576$; $M_0 = 2.8$	RETAS $M_{th} = 2.9$	0.452	0.425	0.398
Feb 8 2014	$b = 0.807$ $p = 1.368$	$N = 598$; $M_0 = 2.8$	RETAS $M_{th} = 4.3$	0.337	0.324	0.296
Feb 9 2014	$b = 0.724$ $p = 2.17$	$N = 778$; $M_0 = 2.6$	RETAS $M_{th} = 4.3$	0.546	0.504	0.467
Feb 10 2014	$b = 0.73$ $p = 2.43$	$N = 801$; $M_0 = 2.6$	RETAS $M_{th} = 4.4$	0.328	0.314	0.277
Feb 11 2014	$b = 0.737$ $p = 2.348$	$N = 813$; $M_0 = 2.6$	RETAS $M_{th} = 4.4$	0.259	0.242	0.216
Feb 12 2014	$b = 0.735$ $p = 1.994$	$N = 825$; $M_0 = 2.6$	RETAS $M_{th} = 4.4$	0.396	0.374	0.349
Feb 13 2014	$b = 0.698$ $p = 1.99$	$N = 944$; $M_0 = 2.5$	RETAS $M_{th} = 4.4$	0.394	0.378	0.338
Feb 14 2014	$b = 0.824$ $p = 1.325$	$N = 669$; $M_0 = 2.8$	RETAS $M_{th} = 3.1$	0.248	0.246	0.23
Feb 15 2014	$b = 0.74$ $p = 2.3$	$N = 877$; $M_0 = 2.6$	RETAS $M_{th} = 4.4$	0.445	0.401	0.375

Table 1 continued

Forecast date	b value	Aftershocks number (N)	Best-fit model	1-Day aftershock occurrence probability of at least one event in the corresponding magnitude range		
	p value	Completeness magnitude (M_0)		M_w 5.0–7.0	M_w 5.0–6.5	M_w 5.0–6.0
Feb 16 2014	$b = 0.745$	$N = 896$; $M_0 = 2.6$	RETAS $M_{th} = 4.4$	0.316	0.293	0.268
	$p = 2.323$					
Feb 17 2014	$b = 0.745$	$N = 912$; $M_0 = 2.6$	RETAS $M_{th} = 4.4$	0.3	0.278	0.248
	$p = 2.345$					
Feb 18 2014	$b = 0.75$	$N = 914$; $M_0 = 2.6$	ETAS $M_{th} = 2.6$	0.171	0.158	0.149
	$p = 1.672$					
Feb 19 2014	$b = 0.751$	$N = 922$; $M_0 = 2.6$	RETAS $M_{th} = 3.1$	0.216	0.203	0.195
	$p = 1.488$					
Feb 20 2028	$b = 0.753$	$N = 931$; $M_0 = 2.6$	ETAS $M_{th} = 2.6$	0.239	0.230	0.211
	$p = 1.568$					
Feb 21 2014	$b = 0.753$	$N = 942$; $M_0 = 2.6$	ETAS $M_{th} = 2.6$	0.204	0.201	0.188
	$p = 1.582$					
Feb 22 2014	$b = 0.754$	$N = 949$; $M_0 = 2.6$	ETAS $M_{th} = 2.6$	0.222	0.202	0.193
	$p = 1.582$					
Feb 23 2014	$b = 0.756$	$N = 960$; $M_0 = 2.6$	RETAS $M_{th} = 2.7$	0.148	0.14	0.131
	$p = 1.542$					
Feb 24 2014	$b = 0.756$	$N = 965$; $M_0 = 2.6$	ETAS $M_{th} = 2.6$	0.131	0.129	0.122
	$p = 1.576$					
Feb 25 2014	$b = 0.759$	$N = 971$; $M_0 = 2.6$	RETAS $M_{th} = 2.7$	0.093	0.093	0.086
	$p = 1.573$					

The last column presents the estimated 1-day probabilities for aftershock occurrence (at least one shock in the selected magnitude range). Here N is the size of the data set on which estimation is based (from the beginning of the sequence until the forecast time)

We verified the consistency of the forecasts with the observed seismicity (Fig. 5). Actually this was done only for the $M_w = 5.0$–6.0 case, because this scenario is the nearest to the real one. In Fig. 5, the performance of the forecast seismicity rates over the observed rates is demonstrated. Although the observed number stays almost always inside the expected variability of the model itself, in general, several important discrepancies are also observed. One of them is associated with the day before the second main shock (of $M_w = 6.0$, see vertical dashed line in Fig. 5), when the simulated number of events significantly exceeds the observed one. It can be considered as a kind of seismic quiescence, without being effective to computationally increase the occurrence probability of the next day strong ensuing earthquake. For the day after, an opposite type of discrepancy is observed—the model has substantially underestimated the observed rate. As expected from the definition of the RETAS model, offered in Sect. 3 and also supported by the results in this analysis, the model is not able to forecast a specific strong event in the sequence (the second strongest event), for which if correctly identified, it should determine the largest occurrence probability. The model is appropriate to depict seismicity evolution in a sequence and to estimate the average number of expected earthquakes in a time magnitude interval.

On the whole, the results in Fig. 5 unclose a slight overestimation derived from the model for nearly all days, most probably due to the estimation of the b value parameter of the Gutenberg–Richter law to the larger magnitudes (Fig. 4), as already commented.

It is a common approach in Seismology to use the cumulative number of events in time (see Ogata 1988; Drakatos and Latoussakis 1996; Gospodinov and Rotondi 2006; Papadimitriou et al. 2013; Karakostas et al. 2014b) for displaying seismicity evolution graphically and to reveal how well a model fits a certain dataset. In this paper, however, we verified the reliability of the forecasts by plotting pairs of occurred events for each day on Fig. 5—forecasted and real, and not cumulative numbers, because values were estimated for different model versions. If we consider the model goodness-of-fit demonstration for the entire 30-day data set, we could do that by plotting expected and real cumulative numbers, which we have done in Fig. 6a. There thick line stands for the expected values, calculated after the best-fit model parameters for the 30-day period (last row in Table 1; see parameter values on Fig. 6a), dotted lines are the error bounds and circles denote the real cumulative number. We have also focused on a 5-day period (dotted rectangle in Fig. 6a), including the second $M_w = 6.0$ event, where a 1-day rate decrease can be identified before this (arrows in Fig. 6b). On the other hand, the latter analysis can be performed in a retrospective manner and our purpose was to imitate a nearly real-time case, grounding on data only until the time of the probability forecast.

Getting back to Fig. 5, it could seem strange that for the first days smaller rates were found than for the next ones, but it should be reminded that the completeness magnitude, M_0, varies with time. It is found equal to $M_0 = 3.2$ for the first 2 days and progressively drops down to $M_0 = 2.5$, resulted to smaller rate for the first days than the later ones (Fig. 5). Marzocchi and Lombardi (2009) used a constant value of $M_0 = 2.5$, but in our study it was difficult to choose a constant completeness magnitude only on catalog data from the first 2 days. We could choose a constant $M_0 = 3.2$; however, a large part of the used data would be lost.

The simulation procedure (step d) requires the definition of the magnitude range for the simulated catalog. The daily completeness magnitude, M_0, was considered as lower

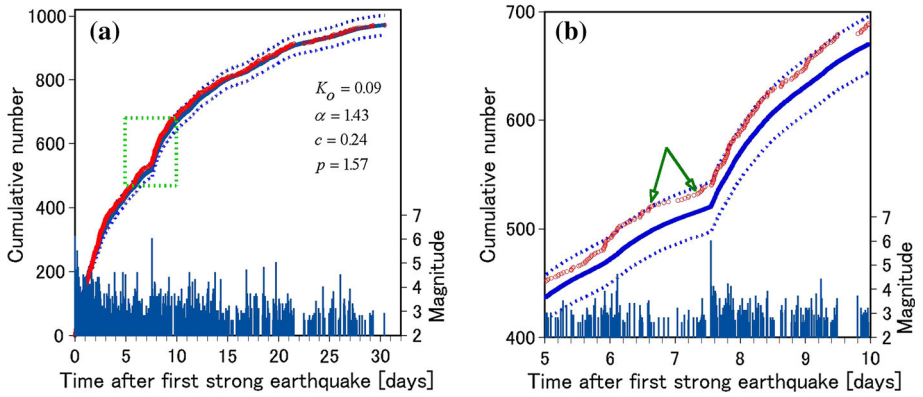

Fig. 6 Expected and real cumulative numbers. *Thick line* stands for the expected values, calculated after the best-fit model parameters for the 30-day period (last row in Table 1), *dotted lines* are the error bounds and circles present the real cumulative number; **a** for the entire 30-day period; **b** enlarged view of the cumulative numbers picture for the period between the 5th and the 10th day, including the second $M_w = 6.0$ event. A 1-day rate decrease can be identified before the strong earthquake (see *arrows*)

magnitude. For the upper magnitude limit, we took into account firstly the area's potential for the maximum expected or maximum observed earthquake, which exceeds $M_w = 7.0$, and thus, this latter value was set as a target for occurrence probability calculations. Earthquakes of $M \geq 6.0$, on the other hand, consist a threat for the area since they are capable to produce severe damage and disturbance to the socioeconomic life, and thus should be included in our targeting earthquake magnitudes. In between the two extremes, the occurrence of $M \geq 6.5$ is also taken as the upper magnitude limit, as representative of more common than $M_w = 7.0$ events and more severe than $M_w = 6.0$ ones. The occurrence probabilities were calculated for at least one event per day in each one of the three magnitude ranges, are given in Table 1 and are plotted against time in Fig. 7, with the dotted line signifying the error bounds for the $M_w = 5.0$–6.0 estimates. All three curves follow the same temporal variations, an indication that this variation depends upon aftershock rate changes alone, with the $M_w = 5.0$–7.0 exhibiting the largest values as they are based on longer magnitude range. The standard deviation at the beginning is small and then noticeably increases, a result attributed to the fact that for the first four samples, the best-fit model found to be the MOF and the simulation was done with much smaller variance than for other versions of the RETAS model (Gospodinov et al. 2007).

Usually the performance of time-dependent models in short-term forecasting is assessed by comparison with long-term seismicity modeled by the stationary Poisson model (Jordan and Jones 2010; Jordan et al. 2011). In this case, the time-dependent models, which capture clustering, yield much higher probabilities than the Poisson model does. When, however, the Poisson model is applied on aftershock data only, assuming stationary rate for the forecast day, then to the contrary, this model will usually produce higher probabilities. This is evidenced in Fig. 7, where the probabilities produced after the assumption of a Poisson distribution for the next day are also shown (upper dashed line).

We later examined the differences between the estimated probability values for the identified completeness magnitudes, compared to the ones for a constant completeness magnitude, for example $M_0 = 2.8$ (Fig. 8). The calculations were performed through the

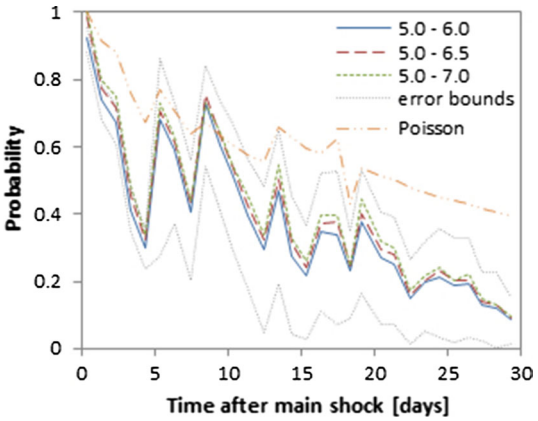

Fig. 7 Daily occurrence probabilities of at least one event in three magnitude ranges, namely $M_w = 5.0$–6.0, $M_w = 5.0$–6.5 and $M_w = 5.0$–7.0, respectively. *Dotted lines* represent error bounds for the $M_w = 5.0$–6.0 case, given by the estimated standard deviation of the simulated rates. The probabilities, produced after the assumption of a stationary Poisson distribution for next day, are also shown (*upper dashed line*). The mean Poisson rate is estimated on all aftershocks until the forecast day

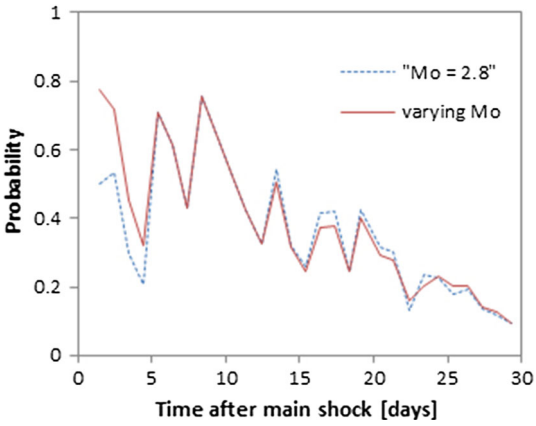

Fig. 8 Estimated probability values of at least one shock in the magnitude range $M_w = 5.0–6.5$ for the determined varying values of M_0 for the different days and for a chosen constant value of the magnitude of completeness $M_0 = 2.8$

best-fit model versions, presented in Table 1, which were identified by varying the domain of the magnitude distribution (by M_0). The probability investigation was done for at least one event in the magnitude range $M_w = 5.0–6.5$, and the results revealed that the probability values changed significantly for the first four samples, when the estimated M_0 values were much higher (3.2, 3.1, 3.1, 3.1, respectively) than the chosen $M_0 = 2.8$. The choice of smaller M_0 value reduced the forecasted probabilities because of the magnitude range increase for the simulated events.

When analyzing the daily occurrence probability, we have to bear in mind that it was calculated after the addition rule in probability theory, which means that this is the total probability for the next 24 h. In fact, the forecast for a certain day is the probability of at least one event in the considered magnitude range for the entire period of the following 24 h, which means that for a shorter period this probability would be different. Figure 9 shows the hourly forecasts for at least one shock in the $M_w = 5.0–6.5$ range. The probability progressively increases, but the increase rate becomes smaller with time. This is due to the rate decay of aftershock occurrence, which was captured by the model.

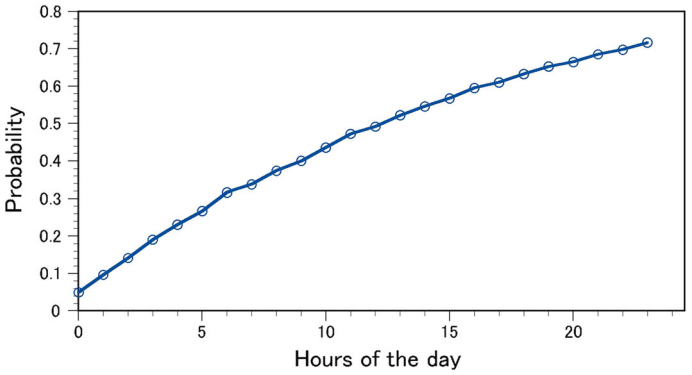

Fig. 9 Hourly probability for the 4th day as an example for the probability variation throughout the day. These probabilities relate to at least one event in the $M_w = 5.0–6.5$ range. Similar relations are valid for all other days

5 Discussion

In this paper, we analyzed some aspects of the occurrence probability calculations of strong aftershocks or new strong events in a sequence. An important contribution, compared to similar papers (Marzocchi and Lombardi 2009; Console et al. 2010; Marzocchi et al. 2012), is the application of the RETAS stochastic model, which provides a number of versions to identify the one best fitting the data, including among them ETAS and MOF as limit cases. We think this is even more important for a case, in which the used model cannot be calibrated on data before the main shock, as it was done by the above authors for Italian sequences. In our case, the model parameters were estimated only on the available aftershock data at the end of each day. At the beginning of the sequence (first four samples), the best-fit model was MOF and our explanation is that the clustering pattern during this period was mainly controlled by the stress changes due to the coseismic slip of the first main shock. The p values for the second and third days are quite low (Table 1), which points to a very slowly decaying aftershock rate, in other words a very intense activity in these first days, an observation already mentioned in the description of the seismic sequence. Then the clustering type changes and starts following the RETAS model ($M_{\text{th}} = 4.3$, $M_{\text{th}} = 3.1$, $M_{\text{th}} = 2.9$), which reveals that randomness in clustering was increased.

As the forecasting procedure required the simulations of the best-fit models, we examined the impact that the selection of magnitude limits for the simulated events had on the forecasts. The choice of the lower limit is rather a technical problem, related to the seismological network detectability, and it is set here equal to completeness magnitude, M_0. The selection of a constant lower limit influences the probability values, depending upon how much the selected lower magnitude differs from M_0. The upper magnitude for the simulation is a matter of choice, which could be made on the earthquake history of the study area, and three alternatives were examined as it was explained in the respective section. The results revealed that larger upper magnitudes resulted to higher probabilities estimates. The general shape of all three curves does not vary significantly, showing quite a similar pattern, which is a good substantiation that the pattern is not due to the chosen magnitude limits, but due to rate changes, well captured by the RETAS model.

The goodness-of-fit verification, which we accomplished for the $M_{\text{w}} = 5.0$–6.5 case, unclosed several important issues. The RETAS model is a stochastic point process describing clustered seismicity due to coseismic stress perturbations. Generally the results revealed that it is applicable to identify the model version, which is best fitting a certain data set and in that way to provide adequate grounds for subsequent probability calculations of strong events occurrence in a sequence. RETAS model is relatively good to forecast observed seismicity rates with a slight overestimation of the simulated rates, due to the deviations in fitting the exponential probability distribution, borrowed from the Gutenberg–Richter law, to the largest magnitude values. All considered models in this paper (RETAS, ETAS, MOF) are developed to model clustering after the assumption that an earthquake occurrence increases the probability of new events in its spatiotemporal vicinity. Under this hypothesis, seismicity features as "quiescence" are not formally incorporated in the modeling. In our analysis, we identified a significant decrease in observed, compared to simulated rate before the second strong main shock in the sequence, which was simply registered since there was not formal possibility for further examination. In general (see Eq. 5), RETAS can be applied to forecast the occurrence probability evolution, but is not principally adept for forecasting the occurrence of a certain large event

(see also Marzocchi and Lombardi 2009), as the AMR and N-C PAST models, which are more suitable for this purpose. The specific feature of the RETAS model is to select the best fit model for a certain sequence by varying Mth. Thus, the model provides the possibility to identify the prevailing type of clustering for the sequence. If the best fit model is the MOF, then events are most probably clustered to only one strong earthquake, if the RETAS model is recognized as best fitting the data, then there should be subclusters, related to other stronger aftershocks and when the ETAS model is providing the best fit of the data, there should be subclusters, following also weak shocks. One could be interested in whether the type of clustering (best-fit RETAS version) is related to certain seismotectonic features of the study area—fault length distribution and possible fault interaction. Eventual answers of these questions require the common examination of many aftershock sequences and seismotectonic information on the affected areas, but these issues are beyond the scope of this study.

In aftershock occurrence probability studies, probability gain factors to be 10–100 or even higher were reported (Jordan and Jones 2010; Jordan et al. 2011) relative to the long-term base model, which is usually time independent and presented by the stationary Poisson distribution. It has to be kept in mind that time-dependent models yield probability gains in short-term forecasts only relative to long-term Poisson seismicity. To the contrary, the application of a Poisson model to aftershock data will result to higher probabilities, as we revealed in this study, because assuming a stationary rate for a certain day, it would normally lead to an overestimation when compared to the usually decaying daily rate.

In addition to the scientific significance, the impact of short-term probability forecasts extends to societal and economic consequences, when they are properly communicating to competent authorities and decision makers. This research area is currently undergoing a huge development concerning models applicability, operational aspects of the obtained results, communication with authorities, etc. In the present study, we have examined the impact of certain calculation parameters on the forecasts and the necessity that each time when occurrence probability values are reported, these parameters should be clearly stated for the reported probabilities to be considered and made compatible with the ones from relevant studies.

Acknowledgments This work was partially supported by the OTRIONS project "Multi-Parametric Network for the Study and Monitoring of Natural Hazards in the Otranto Channel and the Ionian Sea." Some plots were made using the Generic Mapping Tools version 4.5.3 (www.soest.hawaii.edu/gmt, Wessel and Smith 1998). Geophysics Department Contribution 842.

References

Akaike H (1974) A new look at the statistical model identification. IEEE Trans Autom Control AC 19:716–723

Ben-Zion Y, Lyakovsky V (2002) Accelerated seismic release and related aspects of seismicity patterns on earthquake faults. Pure appl Geophys 159:2385–2412

Console R, Murru M, Catalli F (2006a) Physical and stochastic models of earthquake clustering. Tectonophysics 417:141–153

Console R, Rhoades DA, Murru M, Evison FF, Papadimitriou EE, Karakostas VG (2006b) Comparative performance of time-invariant, long-range and short-range forecasting models on the earthquake catalogue of Greece. J Geophys Res. doi:10.1029/2005JB004113

Console R, Murru M, Catalli F, Falcone F (2007) Real time forecasts through an earthquake clustering model constrained by the rate-and-state constitutive law compared with a purely stochastic ETAS model. Seismol Res Lett 78:49–56

Console R, Murru M, Falcone G (2010) Probability gains of an epidemic-type aftershock sequence model in retrospective forecasting of M ≥ 5 earthquakes in Italy. J Seismol 14:9–26
Drakatos G, Latoussakis J (1996) Some features of aftershock patterns in Greece. Geophys J Intern 126:123–134
Gerstenberger M, Wiemer S, Jones L, Reasenberg P (2005) Real-time forecasts of tomorrow's earthquakes for California. Nature 435:328–331
Gerstenberger MC, Jones LM, Wiemer S (2007) Short term aftershock probabilities: case studies in California. Seismol Res Lett 78(1):66–77
Gospodinov DR, Rotondi R (2006) Statistical analysis of triggered seismicity in the Kresna region of SW Bulgaria (1904) and the Umbria–Marche region of central Italy (1997). Pure appl Geophys 163:1597–1615
Gospodinov D, Papadimitriou EE, Karakostas VG, Ranguelov B (2007) Analysis of relaxation temporal patterns in Greece through the RETAS model approach. Phys Earth Planet Int 165:158–175
Gutenberg B, Richter C (1944) Frequency of earthquakes in California. Bull Seismol Soc Am 34:185–188
Holschneider M, Narteau C, Shebalin P, Peng Z, Schorlemmer D (2012) Bayesian analysis of the modified Omori law. J Geophys Res 117:B06317. doi:10.1029/2011JB009054
Jordan TH (2006) Earthquake predictability, brick by brick. Seismol Res Lett 77:3–6
Jordan T, Jones L (2010) Operational earthquake forecasting: some thoughts on why and how. Seismol Res Lett 81:571–574
Jordan TH, Chen Y-T, Gasparini P, Madariaga R, Main I, Marzocchi W, Papadopoulos G, Sobolev G, Yamaoka K, Zschau J (2011) Operational earthquake forecasting; state of knowledge and guidelines for utilization, report by the international commission on earthquake forecasting for civil protection. Ann Geophys. doi:10.4401/ag-5350
Karakostas V, Papadimitriou E, Mesimeri M, Gkarlaouni Ch, Paradisopoulou P (2014a) The 2014 Kefalonia doublet (Mw6.1 and Mw6.0) central Ionian Islands, Greece: Seismotectonic implications along the Kefalonia Transform Fault Zone. Acta Geophys. doi:10.2478/s11600-014-0227-4
Karakostas VG, Papadimitriou EE, Gospodinov D (2014b) Modeling the 2013 North Aegean (Greece) seismic sequence: geometrical and frictional constraints, and aftershock probabilities. Geophys J Int. doi:10.1093/gji/ggt523
Latoussakis J, Stavrakakis G, Drakopoulos J, Papanastassiou D, Drakatos G (1991) Temporal characteristics of some earthquake sequences in Greece. Tectonophysics 193:299–310
Marzocchi W, Lombardi A-M (2009) Real-time forecasting following a damaging earthquake. Geophys Res Lett. doi:10.1029/2009GL040233
Marzocchi W, Murru M, Lombardi A-M, Falcone G, Console R (2012) Daily earthquake forecasts during the May–June 2012 Emilia earthquake sequence (northern Italy). Ann Geophys 55:561–567
McClusky S, Balassanian S, Barka A, Demir C, Georgiev I, Hamburger M, Hurst K, Kahle H, Kastens K, Kekelidze G, King R, Kotzev V, Lenk O, Mahmoud S, Mishin A, Nadariya M, Ouzounis A, Paradisis D, Peter Y, Prilepi M, Reilinger R, Sanli I, Seeger H, Tealeb A, Toksoz MN, Veis G (2000) GPS constraints on crustal movements and deformations in the Eastern Mediterranean (1988–1997): implications for plate dynamics. J Geophys Res 105:5695–5719
Mignan A (2012) Seismicity precursors to large earthquakes unified in a stress accumulation framework. Geophys Res Lett 39:L21308. doi:10.1029/2012GL053946
Mignan A, King G, Bowman D (2007) A mathematical formulation of accelerating moment release based on the stress accumulation model. J Geophys Res 112:B07308. doi:10.1029/2006JB004671
Mogi K (1962) Magnitude-frequency relationship for elastic shocks accompanying fractures of various materials and some related problems in earthquakes. Bull Earthq Res Inst Univ Tokyo 40:831–883
Ogata Y (1988) Statistical models for earthquake occurrences and residual analysis for point processes. J Am Stat As 83:9–27
Ogata Y (1998) Space-time point-process models for earthquake occurrences. Ann Inst Stat Math 50(379–402):597–1615
Ogata Y (2001) Exploratory analysis of earthquake clusters by likelihood-based trigger models. J Appl Probab 38A:202–212
Özel G (2011) A bivariate compound Poisson model for the occurrence of foreshock and aftershock sequences in Turkey. Environmetrics 22(7):847–856. doi:10.1002/env.1098
Papadimitriou EE (2002) Mode of strong earthquake recurrence in central Ionian Islands (Greece). Possible triggering due to Coulomb stress changes generated by the occurrence of previous strong shocks. Bull Seismol Soc Am 92:3293–3308
Papadimitriou EE, Gospodinov D, Karakostas VG, Astiopoulos A (2013) Evolution of the vigorous 2006 swarm in Zakynthos (Greece) and probabilities for strong aftershocks occurrence. J Seismol 17:735–752

Papazachos BC, Papazachou C (2003) The earthquakes of Greece. Ziti Publication, Thessaloniki, p 317
Papazachos BC, Scordilis EM, Panagiotopoulos DG, Papazachos CB, Karakaisis GF (2004) Global relations between seismic fault parameters and moment magnitude of earthquakes. In: 10th international congress of the Hellenic geographical society. Thessaloniki, Greece, 14–17 April 2004, pp 539–540
Reasenberg PA, Jones LM (1989) Earthquake hazard after a mainshock in California. Science 243(4895):1173–1176
Reasenberg PA, Jones LM (1994) Earthquake aftershocks: update. Science 265:1251–1252
Sakkas V, Lagios E (2015) Fault modeling on the early 2014 $\sim$ M6 earthquakes in Cephalonia Island (W. Greece) based on GPS measurements. Tectonophysics. doi:10.1016/j.tecto.2015.01.010
Schorlemmer D, Gerstenberger M, Wiemer S, Jackson DD, Rhoades DA (2007) Earthquake likelihood model testing. Seismol Res Lett 78:17–29
Utsu T (1961) A statistical study on the occurrence of aftershocks. Geophys Mag 30:521–605
Utsu T, Seki A (1955) Relation between the area of aftershock region and the energy of the main shock (in Japanese). Zisin 7:233–240
Wells DL, Coppersmith KJ (1994) New empirical relationships among magnitude, rupture length, rupture width, rupture area, and surface displacement. Bull Seismol Soc Am 84:974–1002
Wessel P, Smith WHF (1998) New, improved version of the generic mapping tools released. EOS Trans AGU 79:579
Wiemer S (2001) A software package to analyze seismicity: ZMAP. Seismol Res Lett 72:373–382